ISSN 1061-3862, International Journal of Self-Propagating High-Temperature Synthesis, 2023, Vol. 32, No. 2, pp. 139–149. © Allerton Press, Inc., 2023.

Influence of NaCl on Magnetic Properties of $MgFe_2O_4$ Nanoparticles Synthesized by Gel Combustion

Y. Orozco[a], A. Betancur[a], E. Chavarriaga[b], J. G. Ramirez[c], R. Moreno[c], J. Palacio[d], S. Leal-Marin[e,f], B. Glasmacher[e,f], O. Gryshkov[e,f], C. Paucar[a], C. Garcia[a], and A. Lopera[a,g,] *

[a] *Grupo de Materiales Cerámicos y Vítreos, Escuela de Física, Universidad Nacional de Colombia, Medellín, 050034 Colombia*

[b] *Departamento de Ciencias Básicas, Universidad Católica Luis Amigó, Medellín, 050034 Colombia*

[c] *Departamento de Física, Universidad de los Andes, Bogotá, 111711 Colombia*

[d] *Institución Universitaria Pascual Bravo, Facultad de Ingeniería, Medellín, 050034 Colombia*

[e] *Institute for Multiphase Processes, Leibniz University Hannover, Garbsen, 30823 Germany*

[f] *Lower Saxony Center for Biomedical Engineering, Implant Research and Development, Hannover, 30625 Germany*

[g] *Grupo de Nanoestructuras y Física Aplicada (NANOUPAR), Dirección Académica, Universidad Nacional de Colombia, Sede de La Paz, La Paz, 202017 Colombia*

** e-mail: aalopera@unal.edu.co*

Received December 15, 2022; revised January 3, 2023; accepted January 11, 2023

Abstract—The effect of sodium chloride (NaCl) on the magnetism of nanopowders of the spinel ferrite ($MgFe_2O_4$) produced using a salt-assisted solution combustion synthesis was investigated. X-ray diffraction (XRD) analysis was conducted to evaluate crystalline structure and phase composition of the synthesized materials. Scanning electron microscopy (SEM) and transmission electron microscopy (TEM) was used to evaluate the particle size and morphology. Magnetic behavior was analyzed by measuring and analyzing the respective hysteresis loops using a vibrating sample magnetometer (VSM). The characterization showed that the presence of NaCl affects the phase composition, size, and dispersion of the nanoparticles, as well as their magnetic behavior. The theoretical size of the nanoparticles was calculated using the Scherrer equation, obtaining sizes of about 21.07 nm for the nanoparticles without salt, 5.90 nm for the sample salt content of 1.7 mol and 6.48 nm—for 3.4 mol. The synthesized nanoparticles showed a drastic decrease in coercivity field, remanence, and saturation with increasing salt content. Therefore, the salt content is a crucial parameter in controlling the morphology and magnetic properties of the nanoparticles obtained by the solution combustion route.

Keywords: gel combustion, magnesium ferrite, superparamagnetism, nanoparticles, spinel

DOI: 10.3103/S106138622302005X

1. INTRODUCTION

$MgFe_2O_4$ is a binary spinel ferrite that belongs to the family of spinel structures with the general formula MFe_2O_4 (M = Zn^{2+}, Co^{2+}, Cu^{2+}, $Ni^{2+,}$ Mg^{2+}, Fe^{2+}, Mn^{2+}) or (AB_2O_4) where A and B are the tetrahedral and octahedral sites of the cations, respectively. The structure is cubic with space group *Fd3m* and is considered a soft magnetic material. The distribution of the cations between the tetrahedral and octahedral sites in the spinel can change the optical, magnetic, and electrical response [1]. $MgFe_2O_4$ is an inverse spinel; when having a nanoscale particle size, it presents an inversion degree [2, 3]. This material has shown a variety of potential applications in the areas of science and engineering, such as supercapacitor manufacturing, microwave devices, humidity sensors, electromagnets, hyperthermia, and antimicrobial response [4–9]. Normally these applications have a direct relationship with the morphology and characteristic structure of the material, i.e., when a few microns or nano-size range particles of $MgFe_2O_4$ are obtained, the magnetic behavior increases considerably; this can be related to a superparamagnetic behavior of each particle generating a fast response to applied magnetic fields with negligible coercivity (the field required to bring the magnetization to zero) and remanence (residual magnetism). These features make superparamagnetic nanoparticles very attractive for a broad range of biomedical applications such as hyperthermia [10, 11]. The key to changing or controlling these properties is the synthesis path. Various methods of synthesis, each one with its advantages and disadvantages, have been used to obtain magnetic materials, such as solvothermal and hydrothermal routes [12, 13], coprecipitation routes [14, 15], solution combustion [16, 17] and specific methods such as Stöber method [18] among others. The selection of the most

suitable synthesis route depends on the requirements for synthesized materials. In the last decades, the solution–combustion route has been used to obtain nanomaterials of different oxides [19–21]. This route is mainly a highly exothermic oxidation–reduction reaction in which oxidizing agents (precursors of the oxide to be obtained generally nitrates) and one or more fuels are used [21]. Some authors report a relationship between the fuel used and the particle size obtained. Specifically, for the synthesis of $MgFe_2O_4$ nanoparticles, sizes between 50 and 100 nm were obtained using urea [22], sizes between 25 to 41 nm using citric acid [23], 60 nm using maleic anhydride as well as using absolute alcohol, 31 nm with EDTA [24], and 57 nm with glycine [16]. Likewise, diverse morphologies highlighting amorphous and cavernous structures and spheres joined by necks have been shown. In term of synthesis of $MgFe_2O_4$, the fuel type directly alters the reaction temperature, which has a very important effect on how Mg^{+2} ions are located in the ferrite's internal structure, thus affecting the material's magnetic response [1]. Using 6-aminohexanoic acid as fuel has the advantage of minimizing the reaction temperature and avoiding steps in the processing. The main attraction of this process is its ability to obtain nano- and micro-structured materials through simple experimental assemblies [3]. One of the unique characteristic properties of the materials obtained by this route is the particle size, which is usually found in micro and nanometric scales beside their high state of aggregation due to high temperatures and release of gases like CO_2, N_2, H_2O vapor, generating necks between particles and porous structures [25]. However, for some applications, fine and stable particles with narrow size distribution are necessary. Thus, it is important to modify the synthesis route in such a way that dispersed and smaller particles are obtained. To achieve this objective, the use of salts can be an alternative, as it has been reported in the formation of dispersed powders of Ce_2O [26], $LaMnO_3$ [27], $ZnFe_2O_4$ [28], $YFeO_3$ [29], $MnFe_2O_4$ [30], hydroxyapatite and chlorapatite [31], $MgAl_2O_4$ [32], Ni/NiO [33], $ZnFe_2O_4$/ZnS [34], Fe_2O_3 [35], and $NiFe_2O_4$ [36]. These salts cover the surface of all the particles and prevent the formation of necks between them, thus avoiding the generation of cavities and modified particles with improved properties.

This paper evaluates the influence of the concentration of NaCl on the magnetic properties of $MgFe_2O_4$ nanostructures obtained in one step using solution combustion synthesis. We characterize the synthesized materials microscopically and structurally and evaluate the superparamagnetic properties and the agglomeration reduction typical in traditional combustion reactions.

2. EXPERIMENTAL

2.1. Synthesis of $MgFe_2O_4$ Nanoparticles

The starting reagents used for the synthesis of magnesium ferrites by the solution combustion route assisted by molten salts were iron nitrate nonahydrate 98% ($Fe(NO_3)_3{\cdot}9H_2O$, PanReac), magnesium nitrate hexahydrate 98% ($Mg(NO_3)_2{\cdot}6H_2O$, Alfa Aesar) as oxidants, 6-aminohexanoic acid 99% ($C_6H_{13}NO_2$, Merck) as fuel, sodium chloride 99.5% (NaCl, Carlo Erba). The fuel/oxidant ratio used in the synthesis (parameter Φ) was set to 0.8 [37]. Equation 1 shows the combustion reaction as a function of the content of salt σ ($\sigma = 0$, 1.7, and 3.4 mol).

$$\begin{aligned} &Mg(NO_3)_2{\cdot}6H_2O + 2Fe(NO_3)_3{\cdot}9H_2O \\ &+ 1.5C_6H_{13}NO_2 + 2.5O_2 + \sigma\,\text{salt} \rightarrow MgFe_2O_4 \\ &+ 9.1CO_2(g) + 4.8N_2(g) + 33.9H_2O(g) + \sigma\,\text{salt}, \end{aligned} \quad (1)$$

Initially, the precursors of magnesium and iron were mixed in an aqueous solution using the minimum amount of water needed to dilute the nitrates. Subsequently, 6-aminohexanoic acid and sodium chloride was added to the solution to achieve a final NaCl concentration of 0, 1.7, and 3.4 mol, respectively. Once the system was solubilized, it was subjected to constant agitation at 350 rpm and a temperature of 180°C until the formation of a gel. At this point, the magnetic agitation was interrupted, and the temperature increased to approximately 250°C followed by the combustion reaction, as shown in Fig. 1. Finally, the powders were recovered and macerated before a final step to remove excess salt used in the reaction by several powder washes, including filtration using a vacuum pump and filter paper.

2.2. Characterization

The crystalline phases of the powders obtained were evaluated by X-ray diffraction (XRD) analysis using a D8 Advance Eco Bruker model diffractometer over the 2θ range between 20° and 80°, step size of 0.02° (2θ) and an accumulated counting time of 0.2 s (Cu K_α radiation, $\lambda = 0.1541$ nm). Raman spectra were obtained at room temperature using a JASCO NRS-3300 spectrometer. A 532 nm Ar ion laser was used as the excitation source, and its power was kept at 10.5 mW. The scanning was done from 100 to 850 cm^{-1}. The morphology and dispersion grade were analyzed by scanning electron microscopy (SEM, EVO MA10 Carl Zeiss microscope) and transmission electron microscopy (TEM, Tecnai F20 Super Twin TMP de FEI). To confirm the superparamagnetic behavior at temperatures above 300 K, hysteresis loops were recorded using a vibrating sample magnetometer (7400-S LakeShore 7400-S Series). The respective parameters such as the saturation magnetization M_s, remanence M_r, coercivity H_c, and squareness ratio SQR were extracted from the hysteresis loops.

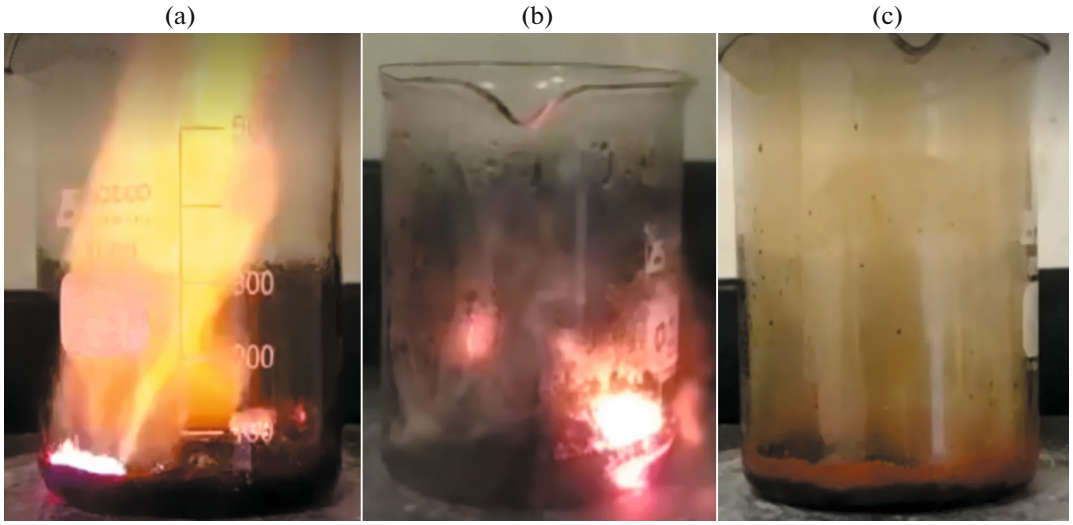

Fig. 1. Photographs of the combustion reaction in the present of different concentrations of NaCl: (a) 0 mol of salt, (b) 1.7 mol of salt, and (c) 3.4 mol of salt. The presence of salt affects the generation of flame and gases during the combustion reaction.

3. RESULTS AND DISCUSSION

An ultrafine powder of reddish-brown color with a clear magnetic response was obtained by solution combustion synthesis. Figure 1 shows the moment when the combustion process occurs.

As the salt ratio increases, the general behavior of the reaction changes. Without salt, a flame of high intensity is formed with the minor release of gases. On the other hand, as the proportion of salt increases, the flame's intensity decreases, which could be associated with the change in the released gases that modifies the atmosphere during the reaction, i.e., the gaseous decomposition products are a mixture of nitrogen oxides, NH_3, and HNCO. These gases are known to be hypergolic in contact with each other once they attain a critical density and the required temperature, they burn with a flame [25, 38]. Furthermore, the flame temperature of the reaction can be estimated, for which a theoretical analysis can be carried out. The theoretical calculations based on thermodynamic consideration help to estimate flame temperature. The adiabatic temperature T_{ad} of the reactions as a function of salt content is calculated by Eq. (2) [25, 28]:

$$Q = -\Delta H^0 = n_{salt}\Delta H_m + \int_{298}^{T} \sum (nC_p)_{products+salt}\, dT, \quad (2)$$

where Q is the heat absorbed by the products and the added salt under adiabatic conditions; n_{salt} and ΔH_m are the molar number and the melting enthalpy of the added salt, respectively; T is the adiabatic flame temperature of the combustion reaction system; C_p is the heat capacity of the products and salt at constant pressure; and $\Delta H°$ is the standard enthalpy of formation expressed by Eq. (3):

$$\Delta H^0_{298} = \sum \Delta H^0_{298}(\text{products}) - \sum \Delta H^0_{298}(\text{reagents}). \quad (3)$$

Using the thermodynamics data provided in Table 1 and obtained from Eqs. (1)–(3), the adiabatic temperatures for the salt variation σ (0, 1.7, and 3.4 mol) were calculated as 1991, 1889, and 1797 K, respectively. This confirms that as the salt content increases, the combustion temperature decreases. This effect can be explained by the fact that the salt absorbs large reaction of the released heat [35]. Even so, the estimated temperatures may be sufficient to obtain $MgFe_2O_4$ in one step [39, 40].

Figure 2 shows the X-ray diffractograms for the powders synthesized with the different molar relations of NaCl (0, 1.7, and 3.4 mol). In the combustion process without salt, we detected the two main phases: magnesium ferrite, indexing with the JCPDS card no. 00-036-0398, and a non-stoichiometric phase of magnesium ferrite, indexing with the JCPDS card no. 01-077-2366. When the content of salt increases, the non-stoichiometric phase vanishes and remains in the magnesium ferrite phase. The increment in the salt proportion affects the broadening of peaks and their width, indicating the decrease in the particle size [41]. Using the Scherrer equation to provide approximate results, the crystallite size of the powder formed by 0, 1.7, and 3.4 mol of NaCl salt was estimated at 21.07, 5.90, and 6.48 nm, respectively, indicating an apparent effect on the size of the particles obtained. This can be associated with the presence of salt. Similar effect was found in synthesis of $ZnFe_2O_4$ using NaCl and KCl salts: increase in salt concentration resulted in decrease in the temperature of the combustion reaction [42]. These results corroborated that the temperatures reached during the salt-assisted combustion

Table 1. Thermodynamic data for the materials in the reaction process

Sample	ΔH^0_{298}, kJ mol^{-1}	ΔH^0_m, kJ mol^{-1}	C_p, J mol^{-1}
$Fe(NO_3)_3{\cdot}9H_2O$	−3285.3	–	–
$Mg(NO_3)_2{\cdot}6H_2O$	−2612.82	–	–
$C_6H_{13}NO_2$	−637.35	–	–
O_2			
$MgFe_2O_4$	−1437.9	–	
CO_2	−393.51	–	$58.17 + 2.72 \times 10^{-3}T$ $58.17 - 0.49 \times 10^{-6}T^2$ $58.17 + 0.04 \times 10^{-9}T^3$
O	0	–	$5.92 + 0.00367T$
H_2O	−241.8	–	$30.09 + 6.83 \times 10^{-3}T$ $30.09 + 6.79 \times 10^{-6}T^2$ $30.09 - 2.53 \times 10^{-9}T^3$
N_2	0	–	$19.51 + 19.89 \times 10^{-3}T$ $19.51 - 8.6 \times 10^{-6}T^2$ $19.51 + 1.37 \times 10^{-9}T^3$
NaCl (s)	–	25.2	$50.72 + 6.67 \times 10^{-3}T$ $50.72 - 2.52 \times 10^{-6}T^2$ $50.72 + 10.16 \times 10^{-9}T^3$
NaCl (l)			$-42.44 + 113.52 \times 10^{-3}T$ $-42.44 - 43.64 \times 10^{-6}T^2$ $-42.44 + 5.89 \times 10^{-9}T^3$

allowed the formation of the magnesium ferrite structures in a one-step reaction.

The spinel phase formation in the nanocrystalline $MgFe_2O_4$ samples is supported by the Raman spectra recorded at room temperature (Fig. 3). Five Raman active modes are expected for the $MgFe_2O_4$ ($A_{1g} + E_g + 3F_{2g}$). The peak around 660–720 cm^{-1} is attributed to A_{1g} due to symmetric stretching of oxygen atoms and metal–oxygen bonds in the tetrahedral coordination AO_4. In comparison, modes below 600 cm^{-1} belong to the motion of the oxygen atoms in octahedral BO_6. It is possible to observe splitting of the peak corresponding to A_{1g} mode; some authors correlate this behavior to the order–disorder effect of two metal ions (Fe^{3+} and Mg^{2+}) over the octahedral and tetrahedral sites that exist in the spinel [7, 43]. However, other authors suggest that this effect is related to the substitution of Fe^{3+} ions by Mg^{2+} ions in the tetrahedral sites and the difference between the mass of Fe^{3+} and Mg^{2+} splits the A1g mode into two branches. The bands observed in the region of 460–640 cm^{-1} were reported to be caused by the predominant stretching vibration associated with the octahedral $Fe^{3+}O_6$ sublattice [44, 45]. Despite this inconsistency, all authors agree that the highest-frequency Raman modes are associated with the tetrahedral sublattice [45]. In the present study we observed that the inclusion of salt in the combustion reaction considerably affects either the order–disorder effect or the degree of substitution of Mg ions.

Scanning electron microscopy (SEM) micrographs were performed to obtain information on the morphology of $MgFe_2O_4$ powders synthesized by the solution combustion route with variation in the salt content. In the structures formed by the combustion reaction in the absence of NaCl (Figs. 4a–4d), the formation of highly aggregated particles representing necks, pores, and cavities was observed. This is mainly due to the accumulation and posterior liberation of typical gases at high temperatures. Once the salt is added, a drastic change in morphology is observed in the synthesized material. Even with only a 1.7 mol salt concentration (Figs. 4e–4h), the absence of pores and cavities can be observed in the structure of the material. Similar behavior was revealed in [27, 30, 32]: gases generated by combustion cannot be lodged internally in the internal structure of the materials present, which forces them to leave the combustion chamber. This agrees with Fig. 1c, in which it is observed that as more salt, less flame is generated, and more gases

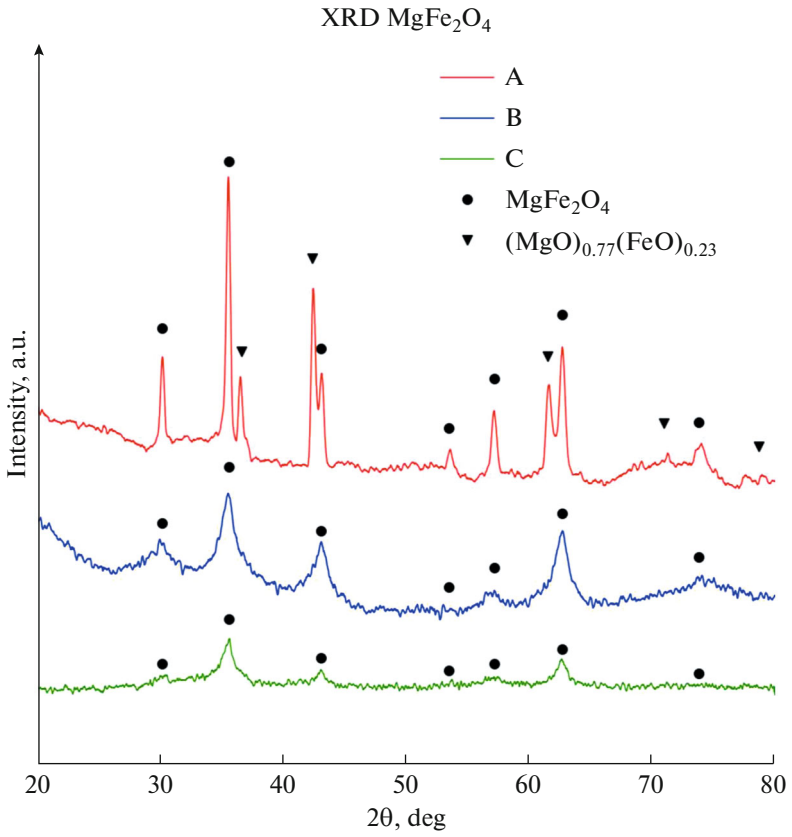

Fig. 2. X-ray diffractograms of $MgFe_2O_4$ obtained by the molten salt-assisted combustion method: (a) 0 mol of salt, (b) 1.7 mol of salt, and (c) 3.4 mol of salt.

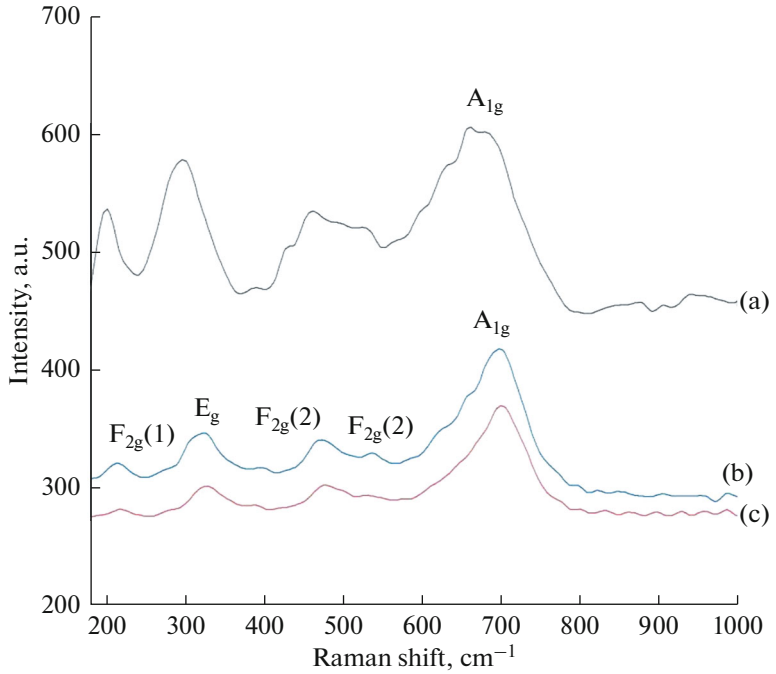

Fig. 3. Raman scattering spectra of $MgFe_2O_4$ obtained by the molten salt-assisted combustion method: (a) 0 mol of salt, (b) 1.7 mol of salt, and (c) 3.4 mol of salt.

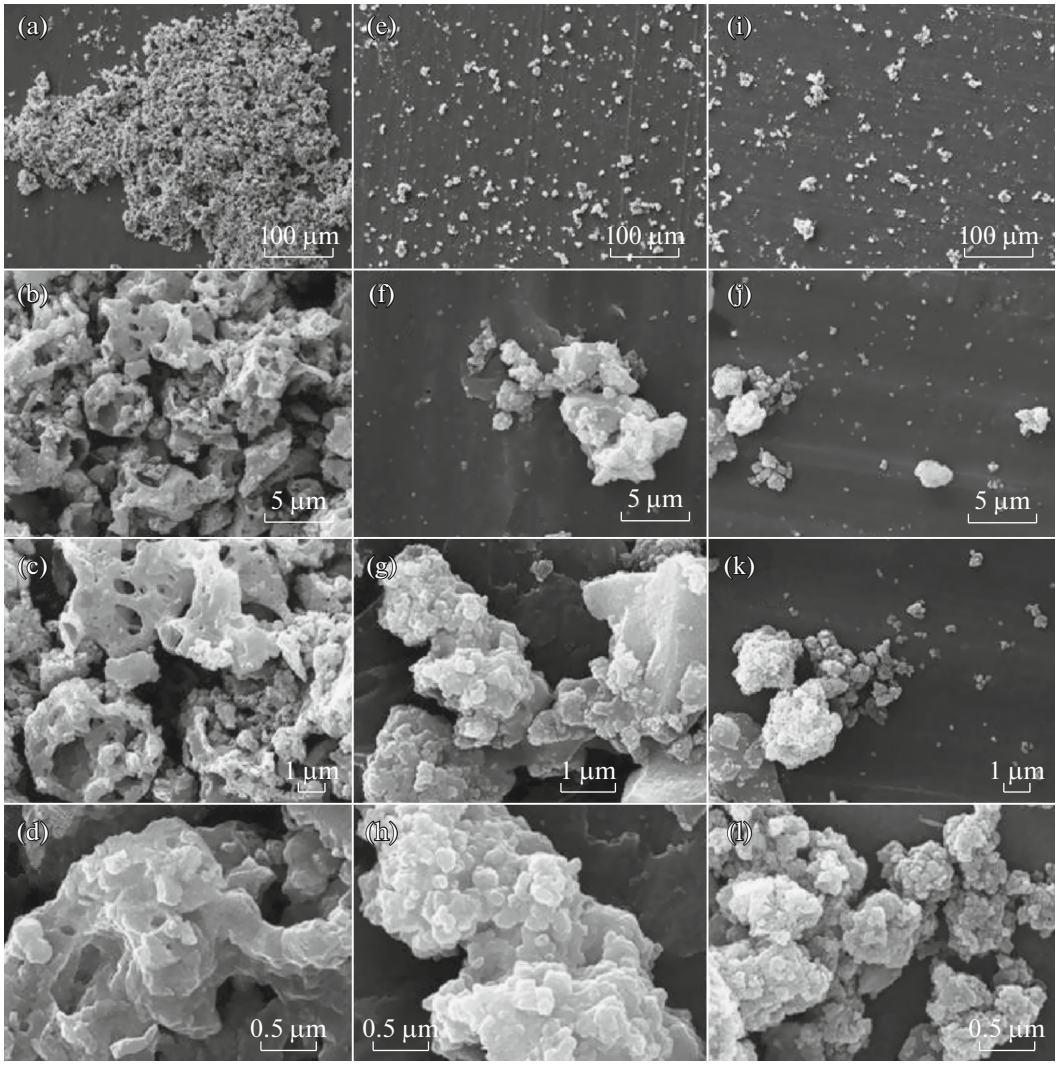

Fig. 4. SEM images of $MgFe_2O_4$ materials at different scales. Each column represents salt content: (a)–(d) without salt; (e)–(h) 1.7 mol; and (i)–(l) 3.4 mol.

release. Nevertheless, we observed certain degree of aggregation, which are composed of smaller solid particles. This effect can be enhanced by increasing salt concentration to 3.4 mol (Figs. 4i–4l). In this case, low aggregation of the particles and their decrease in size was detected. In addition, individual particles can form more extensive complexes. Different authors proposed the possible formation mechanism of well-dispersed nanoparticles produced using the solution combustion approach. Zhang et al. [46] suggested that this process of good dispersion can be associated with the evaporation of the solvent and subsequent precipitation of the salt before combustion protecting the particle formation inside the solvent of the surroundings in such a way that a crust or salt matrix is formed that covers the complex or crystallite that later in the process of combustion does not have contact with other crystallites of the material avoiding the formation of pre-sintering necks typical of combustion processes. Along with a similar mechanism reported by Abbasian et al. [36], the authors found out that once the combustion reaction ends, the salt-coated $MgFe_2O_4$ nanoparticles are trapped into the salt matrix, which prevents the re-agglomeration of the newly formed crystallites and stabilizes the derived nanoparticles. By dissolving the salt and applying washing procedures the agglomerates can be fragmented into smaller particles.

Figure 5 shows TEM micrographics of $MgFe_2O_4$. As shown in Figs. 5a and 5b, inhomogeneous nanoparticles with an irregular shape and agglomerates can be observed in the processes without salt. When the salt (1.7 mol) was added (Figs. 5c–5f), the morphology of particles changed noticeably to quasi-spherical and well–dispersed. These results coincide with the decrease in crystallite observed in the X-ray diffraction and SEM analysis. During combustion, the

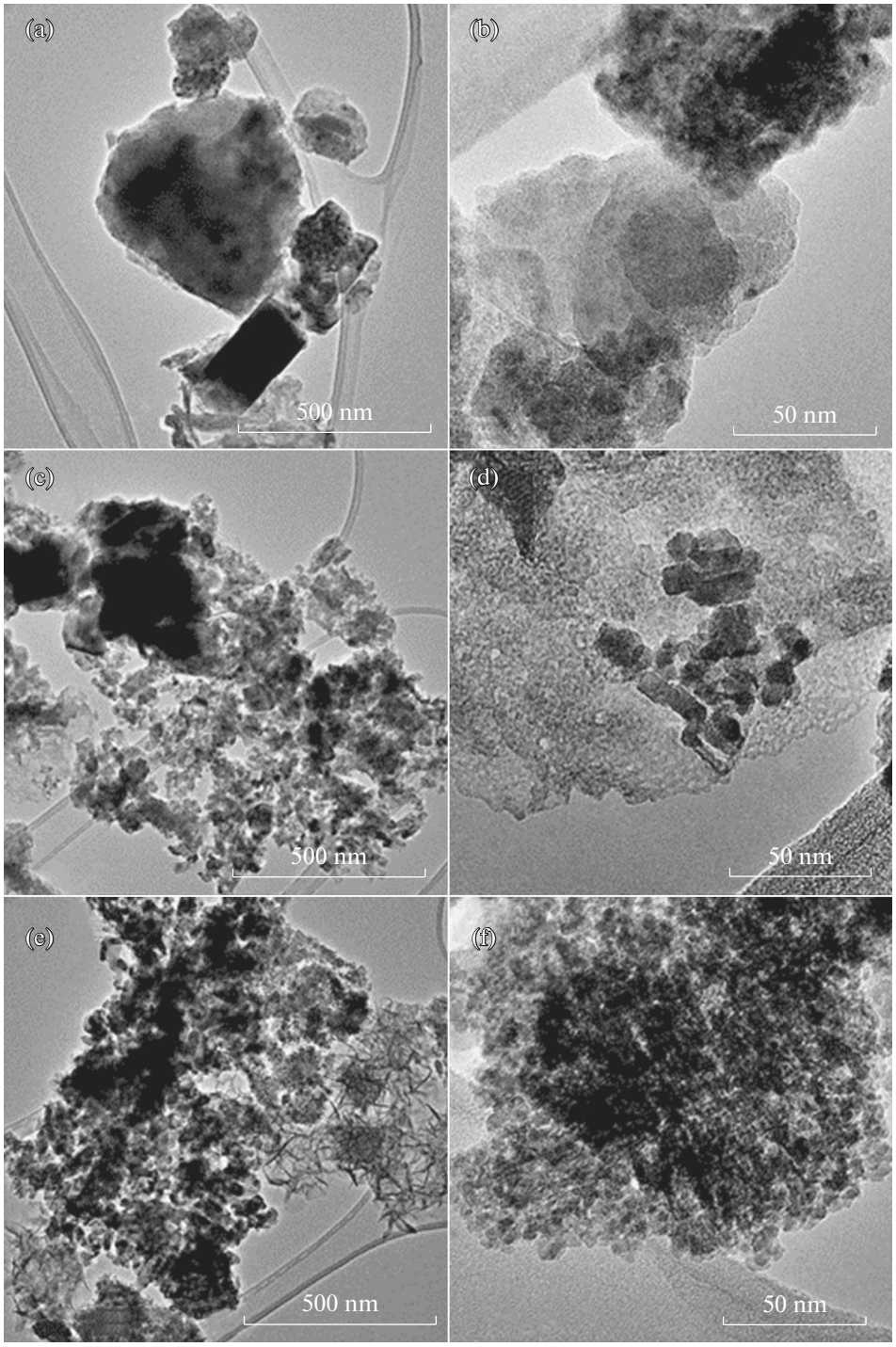

Fig. 5. TEM images of $MgFe_2O_4$ at different scales. Each row represents salt content: (a, b) without salt; (c, d) 1.7 mol; and (e, f) 3.4 mol.

melted salts can deposit between the crystallites, preventing the sintering process and avoiding the formation of the agglomerate.

Magnetization curves of the samples obtained as a result of VSM measurements are shown in Fig. 6. The measured hysteresis loop is typical of soft magnetic material. As can be seen, the addition of salt affects the magnetic properties of synthesized material. The respective magnetization, remanence, and coercivity values were derived from Fig. 6 and shown in Fig. 7. These parameters decrease with increasing salt con-

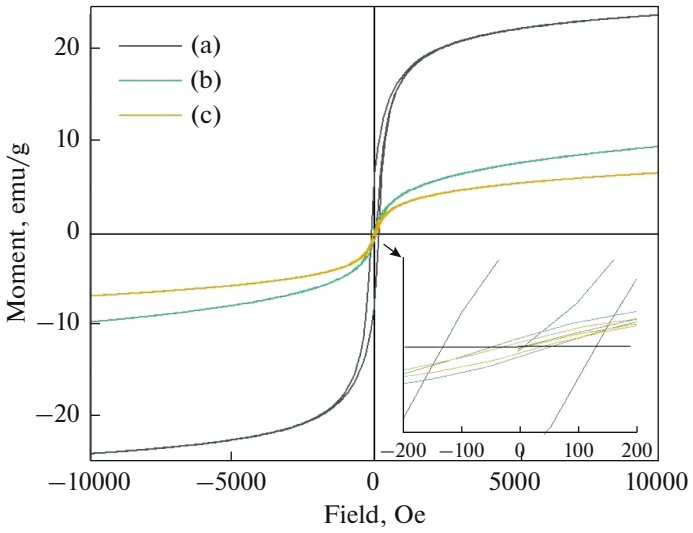

Fig. 6. Magnetic hysteresis loops for salt-assisted synthesized powders in (a) 0, (b) 1.7, and (c) 3.4 mol of salt.

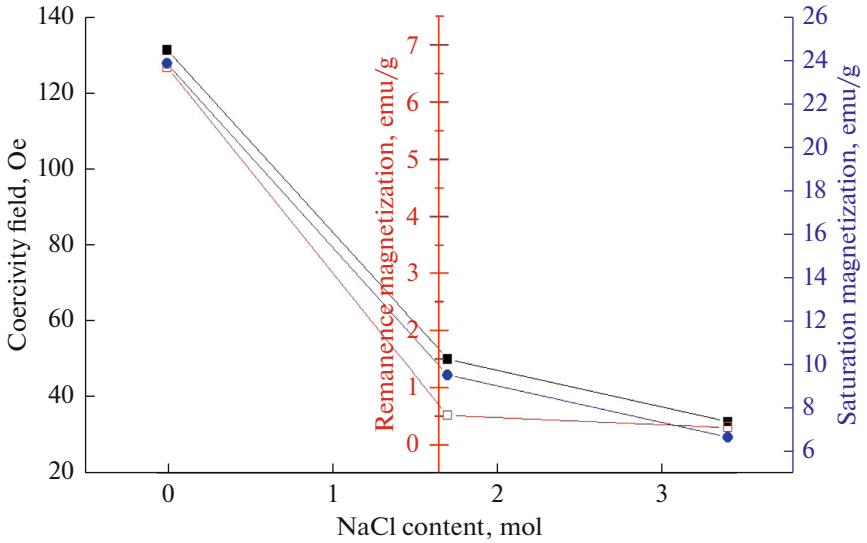

Fig. 7. Effect of NaCl concentration on magnetization, remanence, and coercivity of $MgFe_2O_4$ nanomaterials.

tent, thus suggesting superparamagnetic behavior of nanostructures and single-domain crystals. The value of magnetization for $MgFe_2O_4$ ferrite nanocrystals obtained from combustion synthesis without salt was 23.83 emu/g which is similar to those obtained by other authors using other chemical syntheses [47]. With increasing the salt content in the synthesis from 1.7 to 3.4 mol, the value of magnetization decreased from 9.55 to 6.68 emu/g. This decrease in magnetization could be associated with different mechanisms such as a magnetically dead layer on the surface of the particles, spin glass or grain growth, and A–B exchange interactions [44].

The respective squareness ratio M_r/M_s for the as-prepared powders was calculated based on Fig. 7. This relation allows one to measure the ease with which the direction of magnetization is reoriented towards the nearest axis after removing the field. The values obtained for all powders are 0.27 without salt, 0.27 with 1.7 mol of salt, and 0.07 with 3.4 mol of salt, which indicates that they are soft magnets with superparamagnetism when mol of salt is 3.4 with single magnetic domain particles.

CONCLUSIONS

In this work, we successfully synthesized nanocrystalline $MgFe_2O_4$ powder by the salt-assisted solution combustion method. We revealed the effect of increasing concentration of sodium chloride on morphologi-

cal and structural properties, as well as magnetic behavior of the synthesized materials. Thermodynamic considerations show that calculated values of adiabatic flame decrease with increase in salt content. XRD results revealed that the salt content influences the formation of single-phase $MgFe_2O_4$ beside the size particle of nanocrystalline. Analysis of Raman spectra confirmed the formation of the spinel structure. In turn, SEM and TEM images revealed that the aggregation grade of magnetic ferrite particles diminishes with increasing NaCl content. Hysteresis curves obtained from magnetic measurements indicated the soft nature of the prepared nanoferrites. The increase in the salt concentration decreases the saturation magnetization, coercivity field, and magnetization remanence. This suggests that a superparamagnetic-like behavior was induced, perhaps driven by the nanoparticle morphology changes. Moreover, we demonstrated that the salt content is a crucial parameter for controlling the properties of the magnetic nanoparticles obtained by the solution combustion route.

FUNDING

The authors acknowledge the funding of the German Federal Ministry of Education and Research (BMBF) under the program promotion of scientific and technological cooperation with Colombia (project 01DN21002).

J.G.R. and R.M. Acknowledge suport from Facultad de Ciencias y Vicerrectoría de Investigaciones Universidad de los Andes.

CONFLICT OF INTEREST

The authors declare that they have no conflicts of interest.

REFERENCES

1. Sikalidis, C., *Advances in Ceramics: Synthesis and Characterization, Processing and Specific Applications*, Croatia: InTech, 2011.
2. Mallesh, S., Prabu, D., and Srinivas, V., Thermal stability and magnetic properties of $MgFe_2O_4$@ZnO nanoparticles, *AIP Adv.*, 2017, vol. 7, p. 56103. https://doi.org/10.1063/1.4975355
3. Chavarriaga, E.A., Lopera, A.A., Franco, V., Bergmann, C.P., and Alarcón, J., Gel combustion synthesis and magnetic properties of $CoFe_2O_4$, $ZnFe_2O_4$, and $MgFe_2O_4$ using 6-aminohexanoic acid as a new fuel, *J. Magn. Magn. Mater.*, 2020, vol. 497, p. 166054. https://doi.org/10.1016/j.jmmm.2019.166054
4. Khot, V.M., Salunkhe, A.B., Thorat, N.D., Phadatare, M.R., and Pawar, S.H., Induction heating studies of combustion synthesized $MgFe_2O_4$ nanoparticles for hyperthermia applications, *J. Magn. Magn. Mater.*, 2013, vol. 332, pp. 48–51. https://doi.org/10.1016/j.jmmm.2012.12.010
5. Kang, D., Yu, X., Ge, M., and Song, W., One-step fabrication and characterization of hierarchical $MgFe_2O_4$ microspheres and their application for lead removal, *Microporous Mesoporous Mater.*, 2015, vol. 207, pp. 170–178. https://doi.org/10.1016/j.micromeso.2015.01.023
6. Shakir, I., Sarfraz, M., Ali, Z., Aboud, M.F.A., and Agboola, P.O., Magnetically separable and recyclable graphene–$MgFe_2O_4$ nanocomposites for enhanced photocatalytic applications, *J. Alloys Compd.*, 2016, vol. 660, pp. 450–455. https://doi.org/10.1016/j.jallcom.2015.11.055
7. Narsimulu, D., Rao, B.N., Venkateswarlu, M., Srinadhu, E.S., and Satyanarayana, N., Electrical and electrochemical studies of nanocrystalline mesoporous $MgFe_2O_4$ as anode material for lithium battery applications, *Ceram. Int.*, 2016, vol. 42, pp. 16789–16797. https://doi.org/10.1016/j.ceramint.2016.07.168
8. Reza Barati, M., Selomulya, C., and Suzuki, K., Particle size dependence of heating power in $MgFe_2O_4$ nanoparticles for hyperthermia therapy application, *J. Appl. Phys.*, 2014, vol. 115, p. 17B522. https://doi.org/10.1063/1.4867751
9. Ensafi, A.A., Allafchian, A.R., and Mohammadzadeh, R., Characterization of $MgFe_2O_4$ nanoparticles as a novel electrochemical sensor: application for the voltammetric determination of ciprofloxacin, *Anal. Sci.*, 2012, vol. 28, pp. 705–710. https://doi.org/10.2116/analsci.28.705
10. Chen, Q., Rondinone, A.J., Chakoumakos, B.C., and Zhang, Z.J., Synthesis of superparamagnetic $MgFe_2O_4$ nanoparticles by coprecipitation, *J. Magn. Magn. Mater.*, 1999, vol. 194, pp. 1–7. https://doi.org/10.1016/S0304-8853(98)00585-X
11. Das, H., Debnath, N., Toda, A., Kawaguchi, T., Sakamoto, N., Aono, H., Shinozaki, K., Suzuki, H., and Wakiya, N., Impact of precursor solution concentration to form superparamagnetic $MgFe_2O_4$ nanospheres by ultrasonic spray pyrolysis technique for magnetic thermotherapy, *Adv. Powder Technol.*, 2017, vol. 28, pp. 1696–1703. https://doi.org/10.1016/j.apt.2017.04.007
12. Kurian, J. and Mathew, M.J., Structural, optical and magnetic studies of $CuFe_2O_4$, $MgFe_2O_4$ and $ZnFe_2O_4$ nanoparticles prepared by hydrothermal/solvothermal method, *J. Magn. Magn. Mater.*, 2018, vol. 451, pp. 121–130. https://doi.org/10.1016/j.jmmm.2017.10.124
13. Ali, N.A., Yahya, M.S., Mustafa, N.S., Sazelee, N.A., Idris, N.H., and Ismail, M., Modifying the hydrogen storage performances of $NaBH_4$ by catalyzing with $MgFe_2O_4$ synthesized via hydrothermal method, *Int. J. Hydrogen Energy*, 2019, vol. 44, pp. 6720–6727. https://doi.org/10.1016/j.ijhydene.2019.01.149
14. Akbari, S., Masoudpanah, S.M., Mirkazemi, S.M., and Aliyan, N., PVA assisted coprecipitation synthesis and characterization of $MgFe_2O_4$ nanoparticles, *Ceram. Int.*, 2017, vol. 43, pp. 6263–6267. https://doi.org/10.1016/j.ceramint.2017.02.030
15. Ajeesha, T., Ashwini, A., George, M., Manikandan, A., Mary, J.A., Slimani, Y., Almessiere, M.A., and Baykal, A., Nickel substituted $MgFe_2O_4$ nanoparticles via co-precipitation method for photocatalytic applications, *Phys. B Condens. Matter.*, 2021, vol. 606,

p. 412660.
https://doi.org/10.1016/j.physb.2020.412660

16. Heidari, P. and Masoudpanah, S.M., Structural and magnetic properties of $MgFe_2O_4$ powders synthesized by solution combustion method: the effect of fuel type, *J. Mater. Res. Technol.*, 2020, vol. 9, pp. 4469–4475. https://doi.org/10.1016/j.jmrt.2020.02.07
17. Rúbia, Y.S.Z., Claudir Jr, G.K., Annelise, K.A., and Carlos, P.B., Influence of the fuel composition and the fuel/oxidizer ratio on the combustion solution synthesis of $MgFe_2O_4$ catalyst nanoparticles, *FME Trans.*, 2018, vol. 46, pp. 157–164. https://doi.org/10.5937/fmet1802157Z
18. Fan, H.-T., Liu, X.-G., Xing, X.-J., Li, B., Wang, K., Chen, S.-T., Wu, Z., and Qiu, D.-F., Ordered mesoporous silica cubic particles decorated with silver nanoparticles: a highly active and recyclable heterogeneous catalyst for the reduction of 4-nitrophenol, *Dalton Trans.*, 2019, vol. 48, pp. 2692–2700. https://doi.org/10.1039/C8DT04663H
19. Thoda, O., Xanthopoulou, G., Vekinis, G., and Chroneos, A., Review of recent studies on solution combustion synthesis of nanostructured catalysts, *Adv. Eng. Mater.*, 2018, vol. 20, p. 1800047. https://doi.org/10.1002/adem.201800047
20. Deganello, F. and Tyagi, A.K., Solution combustion synthesis, energy and environment: Best parameters for better materials, *Prog. Cryst. Growth Charact. Mater.*, 2018, vol. 64, pp. 23–61. https://doi.org/10.1016/j.pcrysgrow.2018.03.001
21. Hossain, M.K., Kecsenovity, E., Varga, A., Molnár, M., Janáky, C., and Rajeshwar, K., Solution combustion synthesis of complex oxide semiconductors, *Int. J. Self-Propag. High-Temp. Synth.*, 2018, vol. 27, pp. 129–140. https://doi.org/10.3103/S1061386218030032
22. Rai, A.K., Thi, T.V., Gim, J., and Kim, J., Combustion synthesis of $MgFe_2O_4$/graphene nanocomposite as a high-performance negative electrode for lithium ion batteries, *Mater. Charact.*, 2014, vol. 95, pp. 259–265. https://doi.org/10.1016/j.matchar.2014.06.024.
23. Nguyen, L.T.T., Nguyen, L.T.H., Manh, N.C., Quoc, D.N., Quang, H.N., Nguyen, H.T.T., Nguyen, D.C., and Bach, L.G., A facile synthesis, characterization, and photocatalytic activity of magnesium ferrite nanoparticles via the solution combustion method, *J. Chem.*, 2019, vol. 2019, p. 3428681. https://doi.org/10.1155/2019/3428681
24. He, A., Lu, R., Wang, Y., Xiang, J., Li, Y., and He, D., Adsorption characteristic of congo red onto magnetic $MgFe_2O_4$ nanoparticles prepared via the solution combustion and gel calcination process, *J. Nanosci. Nanotechnol.*, 2017, vol. 17, pp. 3967–3974. https://doi.org/10.1166/jnn.2017.13091
25. Patil, K.C., Hegde, M.S., Rattan, T., and Aruna, S.T., *Chemistry of Nanocrystalline Oxide Materials: Combustion Synthesis, Properties and Applications.* World Scientific, 2008, 364 p. https://doi.org/10.1142/6754
26. Chen, W., Li, F., Yu, J., and Liu, L., A facile and novel route to high surface area ceria-based nanopowders by salt-assisted solution combustion synthesis, *Mater. Sci. Eng. B*, 2006, vol. 133, pp. 151–156. https://doi.org/10.1016/j.mseb.2006.06.020
27. Chen, W., Hong, J., and Li, Y., Facile fabrication of perovskite single-crystalline $LaMnO_3$ nanocubes via a salt-assisted solution combustion process, *J. Alloys Compd.*, 2009, vol. 484, pp. 846–850. https://doi.org/10.1016/j.jallcom.2009.05.059
28. Yang, J., Li, X., Deng, X., Huang, Z., and Zhang, Y., Salt-assisted solution combustion synthesis of $ZnFe_2O_4$ nanoparticles and photocatalytic activity with TiO_2 (P25) as nanocomposite, *J. Ceram. Soc. Japan.*, 2012, vol. 120, pp. 579–583. https://doi.org/10.2109/jcersj2.120.579
29. Chen, Y., Yang, J., Wang, X., Feng, F., Zhang, Y., and Tang, Y., Synthesis $YFeO_3$ by salt-assisted solution combustion method and its photocatalytic activity, *J. Ceram. Soc. Japan*, 2014, vol. 122, pp. 146–150. https://doi.org/10.2109/jcersj2.122.146
30. Zhong, X., Yang, J., Chen, Y., Qiu, X., and Zhang, Y., Synthesis of magnetically separable $MnFe_2O_4$ nanocrystals via salt-assisted solution combustion method and their utilization as dye adsorbent, *J. Ceram. Soc. Japan*, 2015, vol. 123, pp. 394–398. https://doi.org/10.2109/jcersj2.123.394
31. Lopera, A.A., Chavarriaga, E.A., Zuluaga, B., Marin, S., Giraldo, G.O., Estupiñan, H.A., Zapata, V., and Garcia, C.P., Effect of salt concentration on the electrical and morphological properties of calcium phosphates obtained via microwave-induced combustion synthesis, *Adv. Powder Technol.*, 2017, vol. 28, pp. 2787–2795. https://doi.org/10.1016/j.apt.2017.08.007
32. Lee, M.K. and Kang, S., A study of salt-assisted solution combustion synthesis of magnesium aluminate and sintering behaviour, *Ceram. Int.*, 2019, vol. 45, pp. 6665–6672. https://doi.org/10.1016/j.ceramint.2018.12.155
33. Biglari, Z., Alamolhoda, S., and Masoudpanah, S.M., Salt-assisted solution combustion synthesis of Ni and Ni/NiO powders, *J. Supercond. Nov. Magn.*, 2019, vol. 32, pp. 3321–3327. https://doi.org/10.1007/s10948-019-5100-x
34. Abbasian, A.R. and Rahmani, M., Salt-assisted solution combustion synthesis of nanostructured $ZnFe_2O_4$–ZnS powders, *Inorg. Chem. Commun.*, 2020, vol. 111, p. 107629. https://doi.org/10.1016/j.inoche.2019.107629
35. Aali, H., Baygi, N.J., Mollazadeh, S., and Khaki, J.V., Improving the physicochemical properties of NaCl-assisted solution combustion synthesized iron oxide nanoparticles by controlling the thermodynamics of the process, *Ceram. Int.*, 2021, vol. 47, pp. 19315–19327. https://doi.org/10.1016/j.ceramint.2021.03.233
36. Abbasian, A.R., Mahvary, A., and Alirezaei, S., Salt-assisted solution combustion synthesis of $NiFe_2O_4$: Effect of salt type, *Ceram. Int.*, 2021, vol. 47, pp. 23794–23802. https://doi.org/10.1016/j.ceramint.2021.05.086
37. Chavarriaga, E.A., Lopera, A.A., Wermuth, T.B., Arcaro, S., García, C., Alarcón, J., and Bergmann, C.P., Superparamagnetic $MnFe_2O_4$ ferrite by gel combustion synthesis using TRIS as a fuel: Influence of oxidizer to fuel ratio, *Int. J. Self-Propag. High-Temp. Synth.*, 2021, vol. 30, pp. 73–80. https://doi.org/10.3103/S1061386221020059

38. Manukyan, K.V, Cross, A., Roslyakov, S., Rouvimov, S., Rogachev, A.S., Wolf, E.E., and Mukasyan, A.S., Solution combustion synthesis of nano-crystalline metallic materials: Mechanistic studies, *J. Phys. Chem. C*, 2013, vol. 117, pp. 24417–24427. https://doi.org/10.1021/jp408260m

39. Huang, Y., Tang, Y., Wang, J., and Chen, Q., Synthesis of $MgFe_2O_4$ nanocrystallites under mild conditions, *Mater. Chem. Phys.*, 2006, vol. 97, pp. 394–397. https://doi.org/10.1016/J.MATCHEMPHYS.2005.08.035

40. Levy, D., Diella, V., Dapiaggi, M., Sani, A., Gemmi, M., and Pavese, A., Equation of state, structural behaviour and phase diagram of synthetic $MgFe_2O_4$ as a function of pressure and temperature, *Phys. Chem. Miner.*, 2004, vol. 31, pp. 122–129. https://doi.org/10.1007/S00269-004-0380-4/METRICS

41. Jain, I.P., Hydrogen the fuel for 21st century, *Int. J. Hydrogen Energy*, 2009, vol. 34, pp. 7368–7378. https://doi.org/10.1016/j.ijhydene.2009.05.093

42. Inoue, M. and Hirasawa, I., The relationship between crystal morphology and XRD peak intensity on $CaSO_4{\cdot}2H_2O$, *J. Cryst. Growth.*, 2013, vol. 380, pp. 169–175. https://doi.org/10.1016/j.jcrysgro.2013.06.017

43. Padhan, A.M., Rajaitha, P.M., Nayak, S., Hajra, S., Sahu, M., Jagličić, Z., Koželj, P., and Kim, H.J., Synthesis and application of mixed-spinel magnesioferrite: structural, vibrational, magnetic, and electrochemical sensing properties, *Mater. Chem. Front.*, 2022, vol. 7, pp. 72–84. https://doi.org/10.1039/D2QM00628F

44. Chandradass, J., Jadhav, A.H., Kim, K.H., and Kim, H., Influence of processing methodology on the structural and magnetic behavior of $MgFe_2O_4$ nanopowders, *J. Alloys Compd.*, 2012, vol. 517, pp. 164–169. https://doi.org/10.1016/j.jallcom.2011.12.071

45. Tripathi, V.K. and Nagarajan, R., Magnetically separable, bifunctional catalyst $MgFe_2O_4$ obtained by epoxide mediated synthesis, *Adv. Powder Technol.*, 2016, vol. 27, pp. 1251–1256. https://doi.org/10.1016/j.apt.2016.04.013

46. Zhang, X., Jiang, W., Song, D., Sun, H., Sun, Z., and Li, F., Salt-assisted combustion synthesis of highly dispersed superparamagnetic $CoFe_2O_4$ nanoparticles, *J. Alloys Compd.*, 2009, vol. 475, pp. L34–L37. https://doi.org/10.1016/j.jallcom.2008.07.131

47. Naaz, F., Dubey, H.K., Kumari, C., and Lahiri, P., Structural and magnetic properties of $MgFe_2O_4$ nanopowder synthesized via co-precipitation route, *SN Appl. Sci.*, 2020, vol. 2, p. 808. https://doi.org/10.1007/s42452-020-2611-9